

Floor Plan-Guided Visual Navigation Incorporating Depth and Directional Cues

WeiQi Huang¹, Jiaxin Li¹, Zan Wang¹, Huijun Di¹, Wei Liang^{1, 2, †}, Zhu Yang¹

[†] indicates corresponding authors ¹Beijing Institute of Technology, Beijing, China

²Yangtze Delta Region Academy of Beijing Institute of Technology, Jiaxing, China
 {huangweiqi, lijiaxin, wangzan, ajon, liangwei, yangzhu}@bit.edu.cn

Abstract

Guiding an agent to a specific target in indoor environments based solely on RGB inputs and a floor plan is a promising yet challenging problem. Although existing methods have made significant progress, two challenges remain unresolved. First, the modality gap between egocentric RGB observations and the floor plan hinders the integration of visual and spatial information for both local obstacle avoidance and global planning. Second, accurate localization is critical for navigation performance, but remains challenging at deployment in unseen environments due to the lack of explicit geometric alignment between RGB inputs and floor plans. We propose a novel diffusion-based policy, denoted as *GlocDiff*, which integrates global path planning from the floor plan with local depth-aware features derived from RGB observations. The floor plan offers explicit global guidance, while the depth features provide implicit geometric cues, collectively enabling precise prediction of optimal navigation directions and robust obstacle avoidance. Moreover, *GlocDiff* introduces noise perturbation during training to enhance robustness against pose estimation errors, and we find that combining this with a relatively stable Visual Odometry (VO) module during inference results in significantly improved navigation performance. Extensive experiments on the FloNa benchmark demonstrate *GlocDiff*'s efficiency and effectiveness in achieving superior navigation performance, and the success of real-world deployments also highlights its potential for widespread practical applications.

Introduction

Indoor visual navigation has long been a prominent topic in embodied AI research, fostering a wide range of downstream applications, including emergency rescue, assistive robotics, and autonomous exploration. At its core, the task requires agents to navigate through diverse, previously unseen environments toward specified goals using visual observations. These observations, often in the form of RGB or RGB-D images, provide only limited egocentric views of the environment, thereby constraining the agent's ability to plan globally optimal and efficient paths.

To address this limitation, recent work (Li et al. 2021; Ewe et al. 2024; Li et al. 2025; Setalaphruk et al. 2003; Ericson and Jensfelt 2024) has increasingly explored integrating prior floor plans with visual inputs. Floor plans constitute a valuable and widely available source of global spatial knowledge, providing high-level semantic and geometric layouts that re-

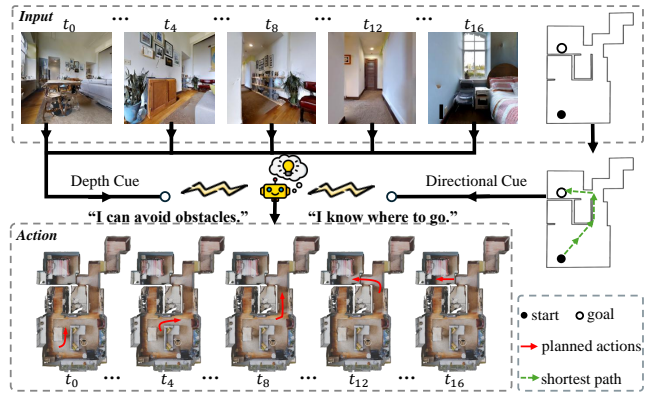


Figure 1: At each time step, our method extracts the depth cue from the observation frames and derives the directional cue by planning the shortest path to the goal on the floor plan. Both complementary cues facilitate the learning of a navigation policy that integrates obstacle avoidance with efficient goal-reaching behavior.

main invariant to dynamic changes such as human activity, temporary obstacles, or furniture rearrangement. This makes them well-suited as priors for supporting localization and navigation in unfamiliar environments. Despite their promise, existing methods still face two key challenges in fully utilizing the structural cues provided by floor plans to guide navigation effectively.

First, due to the inherent modality inconsistency between RGB observations and floor plans, effectively leveraging complementary clues from these two sources to provide local obstacle avoidance and global path planning guidance remains challenging. While prior approaches bypass this challenge by establishing extra topological or semantic maps, combining them with perceptions from LiDAR (Ewe et al. 2024; Li et al. 2021) and inertial measurement units (Goswami et al. 2024), they also introduce increased system costs. FloDiff (Li et al. 2025) directly fuses latent features from floor plans and visual observations using transformer-based encoders, and performs end-to-end navigation within a diffusion policy framework. However, this straightforward fusion approach suffers from low data utilization efficiency and fails to exploit the critical geometric clues inherent in the inputs effectively.

Second, prior work (Li et al. 2021, 2025) has shown that the accuracy of agent localization on the floor plan significantly affects navigation performance. Meanwhile, the spa-

tial geometry misalignment between visual observations and floor plans makes achieving precise localization particularly challenging. Existing studies (Chen et al. 2024; Boniardi et al. 2019; Howard-Jenkins, Ruiz-Sarmiento, and Priscariu 2021) tackle this challenge by matching geometric features from visual observations with boundary features of floor plans. However, these methods often struggle in environments with complex furniture arrangements or repetitive layouts, leading to inaccurate localization.

To address the above challenges, we propose *GlocDiff*, a diffusion-based policy for floor plan-guided visual navigation. The core idea of *GlocDiff* lies in leveraging depth and directional cues from RGB observations and the floor plan, respectively, to guide action generation. As shown in Fig. 1, *GlocDiff* compute the shortest path from the agent’s current location to the goal on the floor plan, which—despite potential intersections with obstacles—serves as a coarse yet informative directional prior. Additionally, *GlocDiff* leverages a pre-trained model (Ke et al. 2024) to produce depth features from RGB observations, enabling a better understanding of local scene geometry and identifying traversable regions, which enables safe navigation in complex environments. The path and depth guidance explicitly exploit geometric clues essential for next-step planning, thus bridging the modality gap inherent in the inputs and improving data efficiency.

Given the reliance of navigation on high-precision localization, we further improve *GlocDiff* in two ways. (i) Unlike previous studies, we employ a standard visual feature-based VO algorithm (Luigi 2025) as the localization module, ensuring more stable and reliable localization throughout the navigation process. (ii) We introduce noise into the current pose and path planning results during training to enhance the model’s robustness to localization inaccuracies.

Extensive experiments on the FloNa (Li et al. 2025) benchmark demonstrate that our approach achieves superior performance even with fewer training pairs, highlighting both its effectiveness and data efficiency. We also conduct comprehensive ablation studies to assess the impact of conditioning on the global shortest path and local depth features, as well as *GlocDiff*’s robustness to varying localization accuracy. Finally, we validate the practical applicability of *GlocDiff* by deploying it on an Automated Guided Vehicle (AGV) without any fine-tuning, showcasing its potential for real-world deployment in embodied systems.

Our contributions are summarized as follows: (1) We propose conditioning the navigation policy on global path planning and local depth features to provide more effective guidance, thus enabling efficient and collision-free navigation. (2) We deploy an online Visual Odometry (VO) system to ensure localization stability and enhance the policy’s robustness by injecting noise into the current pose and shortest path during training. (3) Extensive quantitative and qualitative experiments demonstrate that our method achieves state-of-the-art performance on the FloNa benchmark, and the ablation studies highlight the effectiveness of the proposed designs.

Related Work

Mapping-based Navigation Mapping-based navigation, the prevailing framework, requires building an environmen-

tal map first to support subsequent planning and localization. Typically, VSLAM techniques (Mur-Artal, Montiel, and Tardós 2015; Mur-Artal and Tardós 2017) rely on visual observation inputs to construct sparse metric maps of the surrounding environment. In recent years, more researchers have integrated semantic information into map representations. Previous studies (Chaplot et al. 2020a; Ramakrishnan et al. 2022; Guo et al. 2024; Yu et al. 2024) extract semantic categories from observations, associate the categories with each point in the point cloud, and finally generate a semantic map via differentiable projection operations and a denoising network. Other approaches integrate point-level features (Huang et al. 2023), image features (Pan et al. 2025; Chen et al. 2022; Wang et al. 2023), and panoramic images (Chaplot et al. 2020b) into the built topological graph. VLFM (Yokoyama et al. 2024) iteratively constructs an occupancy map and a value map to guide the agent toward the out-of-view target object. However, the mapping-based method has to explore unseen areas, which tends to be time-consuming for navigation. Moreover, the dynamic nature of objects in indoor environments necessitates real-time updates to the constructed map, making its reuse difficult and significantly reducing efficiency.

Mapless Navigation Without relying on mapping, mapless visual navigation methods directly focus on translating observations into actions. Wijmans et al. (2020) solve the point goal navigation with a near-perfect success rate under idealized settings through large-scale reinforcement learning. Learning-based visual odometry (Partsey et al. 2022; Zhao et al. 2021) is used to address realistic point goal navigation. Recent work also leverages LLMs to guide agents in navigation (Zheng et al. 2024; Chen et al. 2025; Zhou, Hong, and Wu 2024). Leveraging the diffusion policy (Chi et al. 2023), NoMaD (Sridhar et al. 2024) produces collision-free actions and flexibly handles goal-conditioned and goal-agnostic navigation via the goal masking technique. Although mapless methods eliminate the need for mapping, they often make myopic decisions due to the lack of global navigable information.

Navigation with Floor Plan Compared to the two methods mentioned above, floor plan-based navigation eliminates the need for active exploration and instead utilizes the inherent structure and spatial information to perform reliable navigation actions. However, floor plans typically only depict permanent structures such as walls and lack information about obstacles like furniture or other objects. This absence poses challenges for collision-free planning. Setalaphruk et al. (Setalaphruk et al. 2003) extract a Voronoi diagram from the sketch map and subsequently implement localization and navigation based on multiple hypotheses. Li et al. (2021) propose a cognitive navigation solution using floor plans. However, its dependency on pre-collected visual features hinders its practical applicability. To eliminate the dependency, Ewe et al. (Ewe et al. 2024) develop a graph-based navigation framework, enabling navigation without relying on precise scale information. Goswami et al. (2024) leverage stereo-inertial sensors to construct a 2D semantic point cloud, which, in conjunction with the floor plan, enables robot localization

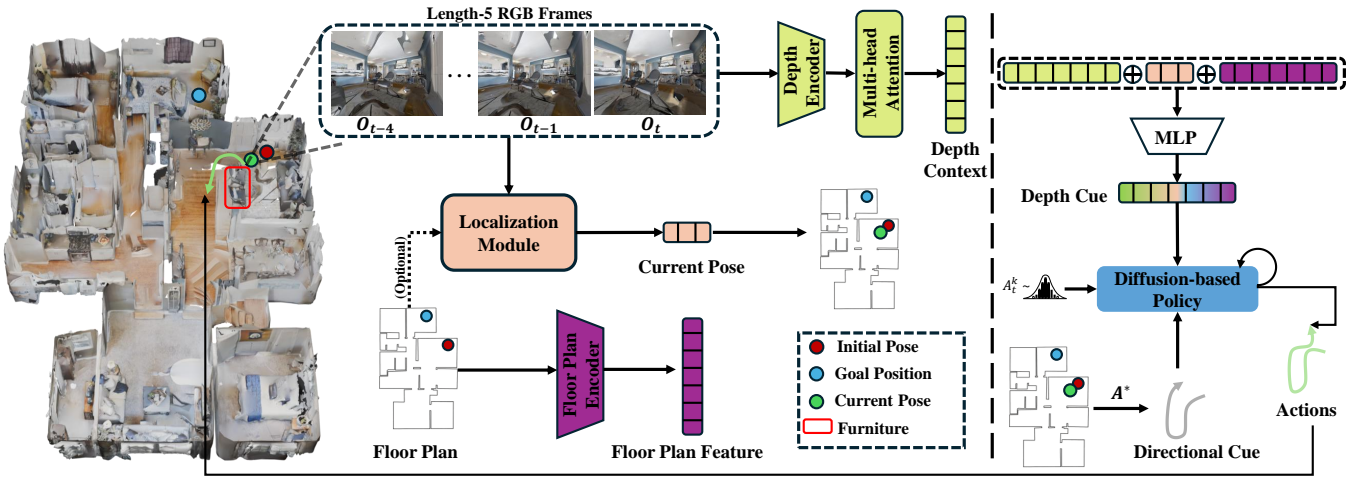


Figure 2: **Overview of *GlocDiff***. The depth encoder uses RGB observations to produce depth latent features, which are fed into a multi-head attention module, yielding the depth context. Taking the depth context, the current pose from the localization module, and the floor plan feature from the floor plan encoder as inputs, the MLP outputs the depth cue. The directional cue is obtained by computing the shortest path to the goal using the A* algorithm. Conditioned on depth and directional cues, the diffusion-based policy generates future actions.

and subsequent navigation. These methods all utilize sensors other than monocular cameras. The closest related work to ours is FloNa (Li et al. 2025), which marks the first attempt to navigate unseen environments using only a monocular camera and a floor plan. FloNa utilizes a transformer-based vision encoder to extract observation context from the floor plan and visual inputs. A diffusion policy (Chi et al. 2023), conditioned on the context, is then employed to generate actions. Although FloNa demonstrates impressive performance, it fails to effectively integrate complementary geometric clues from observations and floor plans. *GlocDiff* tackles this issue by independently processing global and local information to derive two distinct types of guidance.

Diffusion Policy Diffusion-based policies have been successfully applied in various robotic domains, including dexterous manipulation (Simeonov et al. 2023; Chi et al. 2023), locomotion (Huang et al. 2024), and path planning (Sridhar et al. 2024; Li et al. 2025). By framing robot behavior generation as a conditional denoising diffusion process, these policies not only offer high training stability but also ensure temporal consistency by generating coherent action sequences as a whole. Building upon these advances, our work focuses on utilizing diffusion policies conditioned on geometric clues derived from both visual observations and floor plans to achieve vision-based floor plan navigation.

Methodology

As illustrated in Fig. 2, *GlocDiff* extracts a global directional cue from the floor plan and a local depth cue primarily from the RGB observation, which together guide the diffusion policy for future action generation. In the following, we detail each key module of the proposed framework.

Depth Cue Module

To guide *GlocDiff* in generating collision-free actions, the depth cue module processes RGB frames and produces low-dimensional local geometric guidance.

Specifically, we employ a depth encoder (Ke et al. 2024) to extract depth features from RGB images. This encoder utilizes a latent diffusion model to model the conditional distribution $P(\mathbf{d}|\mathbf{o})$, where \mathbf{d} and \mathbf{o} denote the low-dimensional depth feature and RGB observation, respectively. In our model, the depth encoder takes 5 observations as input, including the current observation and the past 4 observations, denoted as $\mathcal{O} = \{o_{t-4}, o_{t-3}, \dots, o_t\}$. Then, the encoder outputs corresponding depth features denoted as $\mathcal{D} = \{d_{t-4}, d_{t-3}, \dots, d_t\}$. These features are then passed through the multi-head attention module (Waswani et al. 2017), and the resulting fused features are averaged to derive the depth context. Subsequently, following (Li et al. 2025), we employ a floor plan encoder consisting of an EfficientNet-B0 (Tan and Le 2019) network and a multilayer perceptron (MLP) to encode the floor plan image, obtaining a floor plan feature. Finally, the depth context, the floor plan feature, and the agent’s pose on the floor plan from the localization module are then concatenated and fed into an MLP to produce the local depth cue, C_t .

Localization Module

In our work, we employ a localization module to determine the current pose of the agent on the floor plan, p_f , using the current ego-centric observations. p_f is represented as $p_f = (q_f, r)$, where $q_f = (x_f, y_f)$ denotes the pixel coordinate on the floor plan, and r represents the orientation. In this task, the floor plan is scaled to the environment, enabling the following equation to relate world coordinates to pixel coordinates:

$$p_w = (q_w, r) = (\mu \times x_f + \delta_x, \mu \times y_f + \delta_y, r), \quad (1)$$

where μ denotes the floor plan resolution (*i.e.*, physical distance per pixel) and δ represents the offset.

During training, we use the ground truth (GT) poses from FloNa (Li et al. 2025) as the localization results. For testing and deployment, we utilize a visual odometry or a floor plan-based visual localization module to estimate the current pose.

Directional Cue Module

The directional cue module provides the policy with global shortest path guidance. Specifically, we employ the A* algorithm to compute the shortest path from the current position to the target within the floor plan. The path is represented as $\mathcal{T}_s = \{q_{f,0}, q_{f,1}, \dots, q_{f,i}, \dots, q_{f,t}\}$, where $q_{f,0}$ denotes the pixel coordinates of the current position and $q_{f,t}$ corresponds to the target point. Then, we convert each point in \mathcal{T}_s into metric coordinate using μ and δ in Eq. (1), represented as $\mathcal{T}_{w,s} = \{q_{w,0}, q_{w,1}, \dots, q_{w,i}, \dots, q_{w,t}\}$. Next, we transform each point in $\mathcal{T}_{w,s}$ to the current agent coordinate system by utilizing the formula

$$q_{a,i} = (q_{w,i} - q_{w,0}) \cdot R, \quad (2)$$

resulting in $\mathcal{T}_{a,s} = \{q_{a,0}, q_{a,1}, \dots, q_{a,i}, \dots, q_{a,t}\}$. Here, $R = \begin{pmatrix} \cos r_0 & -\sin r_0 \\ \sin r_0 & \cos r_0 \end{pmatrix}$, r_0 denotes the orientation of the first point in the shortest path. In the agent coordinate system, the agent's current position serves as the coordinate origin, the current orientation aligns with the positive X-axis, while the leftward direction aligns with the positive Y-axis. Notably, we assume the agent does not experience height variation during navigation, and thus, we only consider a 2D coordinate system (without the Z-axis). Finally, we empirically take the first 32 points of $\mathcal{T}_{a,s}$ (about 1.2 m) as the path guidance C_g .

Diffusion Policy

Diffusion policy (Chi et al. 2023) leverages the Denoising Diffusion Probabilistic Models (DDPMs) (Ho, Jain, and Abbeel 2020) to formulate visuomotor robot policies. In our work, using the depth and directional cues, C_l and C_g , the diffusion policy learns to approximate the conditional distribution $P(A_t | C_l, C_g)$ through a forward and reverse process, where A_t is a 32×2 vector representing the generated sequence of future 32 actions at time step t . Each action corresponds to an approximate movement of 4 cm, and the agent executes the first 20 steps (*i.e.*, around 0.8 cm) of the predicted sequence during deployment.

In the forward process, diffusion policy iteratively adds Gaussian noise and converts the A_t^0 to A_t^K , where A_t^0 is the initial action sequence, and K is the total steps. The entire process is given by $P(A_t^{1:K} | A_t^0) = \prod_{k=1}^K P(A_t^k | A_t^{k-1})$.

In the reverse process, diffusion policy learns the conditional distribution $P(A_t^{k-1} | A_t^k, C_l, C_g)$. Specifically, the diffusion policy employs a noise prediction network of UNet (Ronneberger, Fischer, and Brox 2015) architecture to predict the added noise, ϵ' , and utilizes the noise scheduler to carry out the denoising operation. The process can be described as:

$$\epsilon' = \varepsilon_\theta(A_t^k, C_l, C_g, k), \quad (3)$$

$$A_t^{k-1} = \mathcal{S}(\epsilon', A_t^k, k), \quad (4)$$

where ε denotes the noise prediction network with parameters θ and \mathcal{S} is the DDPM noise scheduler.

As shown in Fig. 3, our noise prediction network includes three downsample modules, one bottleneck module, two upsample modules, and a 1D convolutional layer. Each module consists of several 1D convolutional blocks, activation functions, and residual connections. The network takes noisy

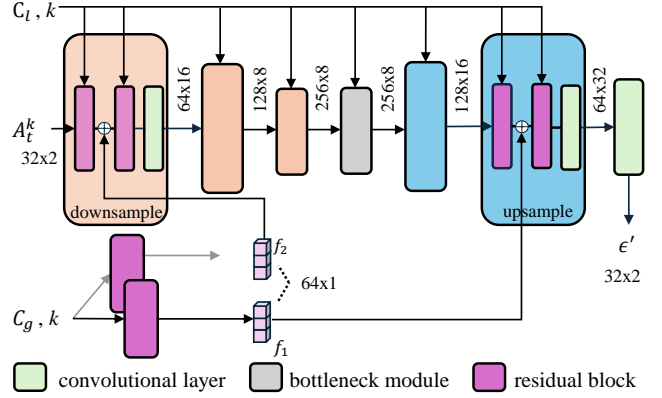


Figure 3: **Conditional UNet**. The directional cue and the time step are fed into the first down module and the second up module, while the depth cue and the time step are fed into each module.

actions of size 32×2 , along with depth and path guidance, C_l and C_g , as input and outputs a predicted noise of size 32×2 . C_l and the time step serve as inputs to each module. Meanwhile, C_g and time step are first processed through two identical residual blocks, producing two features: f_1 and f_2 . f_1 is added to the output of the first residual block in the final upsample module, while f_2 is added to the output of the first residual block. Notably, we apply positional encoding to the time step before feeding it into the network. During training, we use the following loss function:

$$\mathcal{L} = \text{MSE}(\epsilon, \epsilon'), \quad (5)$$

where $\text{MSE}(\cdot)$ denotes the mean square error function, and ϵ denotes the added noise at the forward process. During inference, our model iteratively predicts and removes noise to recover a clean action sequence A_t^0 from Gaussian noise.

Training

We use the data provided by FloNa (Li et al. 2025), collected from 67 Gibson simulation environments. Each scene contains 150, 180, or 200 episodes, depending on the scene size, resulting in a total of 20, 214 episodes. We sample training data from this dataset, with each sample consisting of five consecutive frames, the current and goal positions, and a floor plan image.

To improve the model's robustness to localization noise, we introduce perturbations to both the shortest path \mathcal{T}_s and the ground truth current pose p_w during training. Specifically, we perturb the shortest path using the following formula:

$$\mathcal{T}_n = \mathcal{T}_s + u, \quad (6)$$

where \mathcal{T}_n denotes noisy path and $u \sim \mathcal{U}(0, B)$ represents the perturbation. B represents the upper bound of the perturbation, which increases with each epoch i , as shown by the following formula:

$$B_i = \alpha \cdot \sin\left(\frac{i}{N} \cdot \frac{\pi}{2}\right), \quad (7)$$

where α is the maximum perturbation value, while N represents the total epochs. Meanwhile, we add Gaussian noise, $n_p \sim \mathcal{N}(0, 0.1)$ and $n_r \sim \mathcal{N}(0, \frac{\pi}{36})$, to the ground truth position and orientation.

Table 1: The details of the baselines with respective localization and planning modules, as well as training data size.

Model	Localization	Planner	Train Set Size
Loc-A* (GT)	GT Pose	A*	-
Loc-FloDiff (F ³) (Li et al. 2025)	F ³ Loc (Chen et al. 2024)	Loc-FloDiff	180M
Loc-FloDiff (GT) (Li et al. 2025)	GT Pose	Loc-FloDiff	180M
GlocDiff (F ³)	F ³ Loc	GlocDiff	1.2M
GlocDiff (GT)	GT Pose	GlocDiff	1.2M
GlocDiff (VO)	Visual Odometry	GlocDiff	1.2M

Implementation

In our implementation, the multi-head attention consists of four heads, each with four layers. We choose Square Cosine Noise Schedule (Nichol and Dhariwal 2021) to train the diffusion policy. We use the AdamW optimizer, with the learning rate controlled by PyTorch’s CosineAnnealingLR scheduler. The maximum learning rate is set to 0.0001, and the maximum number of iterations is 20. We set α to 0.1. The training of *GlocDiff* is performed on 8 NVIDIA 4090 GPUs, with a batch size of 64 per GPU. *GlocDiff* is trained for $N = 20$ epochs and reaches convergence.

Experiments

To evaluate our approach thoroughly, we conduct extensive experiments within the simulation environment, including baseline comparisons and ablation studies. Furthermore, we deploy our policy on a real AGV, demonstrating its practical utility, robustness, and generalization capabilities in real-world settings.

Main Experiments

Setup We conduct our experiments in the Gibson (Xia et al. 2018) simulator. The testing episodes are sourced from FloNa (Li et al. 2025), comprising fifty unseen scenes, with each scene containing ten episodes. To ensure safe navigation, we check whether the proposed action would cause a collision before execution. If so, we intervene by instructing the agent to perform a 45° left turn and re-plan a new action sequence. The navigation is deemed successful if the final agent position falls within τ_d meters of the goal and the total number of interventions does not exceed τ_c .

In our experiments, we select six baselines, with their specific components outlined in Tab. 1. Both Loc-FloDiff (F³) and *GlocDiff* (F³) employ F³Loc (Chen et al. 2024), an SOTA end-to-end floor plan localization model, as their localization module. Both Loc-FloDiff (GT) and *GlocDiff* (GT) use the ground truth (GT) pose as localization results. The Loc-A* (GT) leverages ground-truth localization and directly follows the shortest path computed by the A* algorithm on the floor plan. In *GlocDiff* (VO), a VO algorithm (Luigi 2025) is used to track the agent’s pose, serving as the localization module. Due to the lack of scale information, we manually set the scale to 0.04m, based on the average inter-frame displacement in our dataset.

Unlike the dense sampling strategy used for collecting data when training Loc-FloDiff, we sample every five frames to ensure that each observation in a trajectory is sampled only once. As a result, *GlocDiff* is trained on 1.2 million samples, whereas Loc-FloDiff is trained on 180 million samples. For evaluation, we adopt Success Rate (SR) and Success Weighted by Path Length (SPL) as our metrics. We evaluate

all baselines using the distance threshold values (τ_d) of 0.25, 0.30, and 0.35, as well as the intervention count values (τ_c) of 10, 30, 50, and ∞ .

Quantitative Results Tab. 2 presents the quantitative results on the FloNa test set. We discuss three key observations:

- *GlocDiff* demonstrates a consistent and substantial performance improvement over both Loc-FloDiff and Loc-A* in terms of SR and SPL, irrespective of whether ground-truth or estimated poses are employed. This performance gap becomes increasingly pronounced under stricter thresholds of τ_d and τ_c . Such notable gains underscore *GlocDiff*’s ability to effectively exploit the complementary nature of floor plan priors and visual observations, thereby markedly enhancing the agent’s capacity for obstacle avoidance and efficient path planning.
- When the localization results shift from GT poses to predictions from the F³Loc module, Loc-FloDiff experiences a significant decline in performance, with the SR dropping in the range of 34.2% to 47.8% and the SPL dropping in the range of 32.38% to 43.60%. In contrast, the performance of *GlocDiff* shows a more moderate decline, with the SR falling by 28.20% to 39.80% and the SPL decreasing by 28.56% to 32.68%. This highlights that our model exhibits greater robustness to localization noise.
- The SR of *GlocDiff* (VO) is approximately 50% higher than that of *GlocDiff* (F³), indicating that visual odometry (VO) is a more suitable localization module for floor plan navigation compared to F³Loc. Since VO can continuously track the agent’s pose, it remains relatively stable for indoor navigation tasks, despite cumulative errors. In contrast, F³Loc maps observations to poses, introducing room-level errors, which are unacceptable for floor plan navigation. We quantitatively evaluate the localization accuracy of both VO and F³Loc to support this claim; please refer to the supplementary material for details. Moreover, as the τ_c increases, the SPL gap between *GlocDiff* (VO) and *GlocDiff* (GT) gradually narrows, indicating the accumulated error of VO does not significantly affect the planning ability.

Qualitative Results Fig. 4 visualizes the trajectories of different models across six episodes.

Ablation Study

Ablation Study on Depth and Directional Cues We further evaluate the effects of different guidance on the policy. To assess the impact of the local depth guidance, we use an EfficientNet to directly encode the RGB observations, obtaining RGB context to replace the original depth context, while keeping other design aspects consistent with those of *GlocDiff*. The resulting ablation model is denoted as w/o depth. To analyze the influence of the directional guidance, we directly utilize the target point to replace the shortest path, while also keeping other aspects consistent with *GlocDiff*. This modification results in another ablation model, referred to as w/o path. The two models described above are both trained for 20 epochs and reach convergence. We evaluate SR, SPL, and the mean Number of Collisions (NoC) of two models using GT poses.

Table 2: Performance of different baselines under various thresholds. Bold numbers indicate the best results.

Method	Loc-FloDiff (F ³)			GlocDiff (F ³)			GlocDiff (VO)			Loc-A* (GT)			Loc-FloDiff (GT)			GlocDiff (GT)			
	τ_c	$\tau_d(m)$			$\tau_d(m)$			$\tau_d(m)$			$\tau_d(m)$			$\tau_d(m)$					
		0.25	0.30	0.35	0.25	0.30	0.35	0.25	0.30	0.35	0.25	0.30	0.35	0.25	0.30	0.35	0.25	0.30	0.35
SR(%) \uparrow	10	4.80	6.00	6.40	53.40	56.00	57.80	68.60	69.80	70.20	16.60	25.40	38.60	39.00	44.20	44.60	79.60	80.40	80.60
	30	11.60	14.00	15.00	69.20	70.00	71.80	80.80	82.20	82.80	18.20	28.40	43.80	53.40	60.80	61.00	92.80	92.80	93.20
	50	17.80	20.60	22.40	77.80	78.80	80.60	86.60	87.60	87.80	18.50	29.40	45.60	59.20	68.40	68.40	94.20	94.20	94.20
	∞	26.80	30.80	33.00	86.40	87.40	89.40	89.80	90.40	90.60	18.60	29.60	45.80	66.00	75.80	76.00	97.60	97.60	97.60
SPL(%) \uparrow	10	4.02	5.24	5.54	41.67	45.08	46.85	52.88	55.51	56.98	16.50	25.30	38.51	36.30	41.40	42.10	62.62	64.85	66.44
	30	6.40	8.25	8.98	49.35	52.35	54.16	59.07	61.91	63.59	18.10	28.30	43.51	44.10	50.40	51.20	70.38	72.57	74.06
	50	8.07	9.98	10.80	52.61	55.77	57.55	61.31	63.90	65.50	18.50	29.30	45.11	46.60	53.40	54.10	70.98	72.98	74.48
	∞	9.58	11.70	12.50	54.77	57.94	59.75	62.57	65.04	66.64	18.50	29.40	45.31	48.20	55.20	56.00	72.36	74.36	75.86

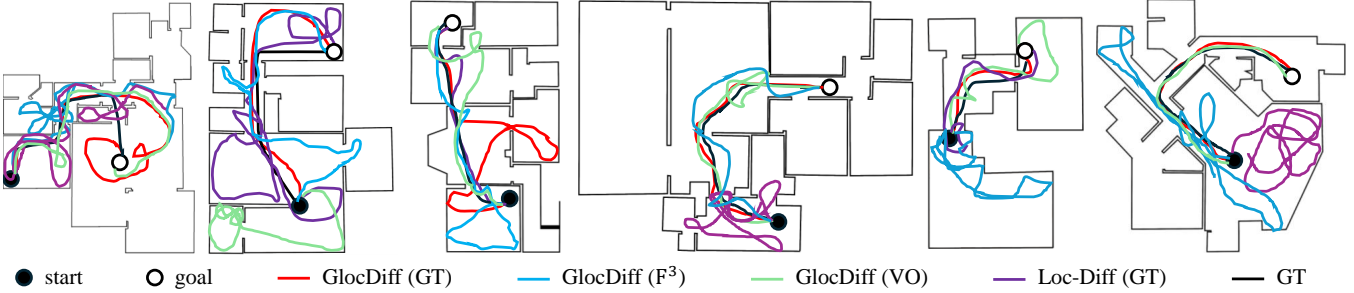


Figure 4: Trajectory visualization. The visualization of trajectories for four baselines across six episodes.

Table 3: Ablation results. Bold and underlined numbers indicate the best and second-best results, respectively.

Model	τ_c	w/o depth				w/o path				GlocDiff (GT)			
		$\tau_d(m)$				$\tau_d(m)$				$\tau_d(m)$			
		0.25	0.30	0.35	0.40	0.25	0.30	0.35	0.40	0.25	0.30	0.35	0.40
SR(%) \uparrow	10	64.20	65.00	66.40	66.80	70.60	71.40	72.40	72.80	79.60	80.40	80.60	80.80
	30	81.00	81.60	82.80	83.00	82.00	82.40	83.00	83.20	92.80	92.80	93.20	93.20
	50	<u>85.60</u>	<u>87.00</u>	<u>88.00</u>	<u>88.20</u>	85.00	85.60	86.00	86.20	94.20	94.20	94.20	94.20
	∞	<u>92.20</u>	<u>93.00</u>	<u>93.40</u>	<u>93.40</u>	89.00	89.40	89.60	89.80	97.60	97.60	97.60	97.60
SPL(%) \uparrow	10	47.22	49.83	52.20	53.60	50.44	52.74	<u>54.84</u>	<u>55.90</u>	62.62	64.85	66.44	67.71
	30	<u>55.98</u>	<u>58.70</u>	<u>60.98</u>	<u>62.40</u>	55.90	58.07	60.09	61.21	70.38	72.57	74.06	75.34
	50	<u>58.07</u>	<u>60.84</u>	<u>63.11</u>	<u>64.58</u>	57.24	59.49	61.42	62.54	70.98	72.98	74.48	75.76
	∞	<u>60.15</u>	<u>62.93</u>	<u>64.90</u>	<u>66.30</u>	58.51	60.71	62.53	63.66	72.36	74.36	75.86	77.16
NoC \downarrow	10	4.46	4.34	4.23	4.17	<u>3.70</u>	<u>3.63</u>	<u>3.52</u>	<u>3.49</u>	3.09	2.99	2.95	2.89
	30	9.46	9.19	8.84	8.71	<u>7.87</u>	<u>7.77</u>	<u>7.54</u>	<u>7.46</u>	5.38	5.16	5.10	5.01
	50	12.66	12.19	11.63	11.45	<u>11.06</u>	<u>10.96</u>	<u>10.63</u>	<u>10.51</u>	6.65	6.39	6.34	6.24
	∞	<u>21.78</u>	<u>20.41</u>	<u>19.61</u>	<u>19.42</u>	31.93	31.82	31.06	30.41	10.81	10.55	10.49	10.39

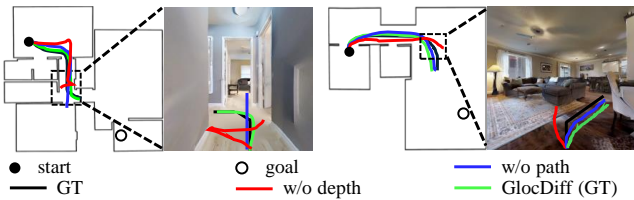


Figure 5: Performance of different baselines on the test episodes in Mobridge (left) and Spotswood (right). The left column illustrates the traversed trajectory, while the right column showcases the diverse actions generated by different models based on the same observation.

As outlined in Tab. 3, *GlocDiff* (GT) achieves the best performance across all cases. Three key conclusions can be drawn. First, the removal of either the local guidance or the global guidance significantly degrades the model’s perfor-

mance. This indicates that both global and local guidance contribute to enhancing the robot’s ability to navigate safely in complex environments. Specifically, the global guidance provides essential support for efficient navigation across the floor plan, while the local guidance improves the understanding of the scene’s geometric structure, thereby aiding in the identification of traversable regions. Second, the performance of the w/o depth model is lower than that of the w/o path model under low τ_c thresholds in terms of SR and SPL, but the trend reverses as the threshold increases. This indicates that removing depth features impairs the agent’s ability to avoid obstacles, which in turn leads to more frequent interventions and reduced performance at lower τ_c thresholds. However, as the intervention threshold increases, planning ability becomes more critical, leading to a performance drop for the w/o path model due to the lack of global planning



Figure 6: **Three real-world test episodes.** The left columns present the top-down view of successful episodes, with 1 and 5 indicating the start and goal positions. The right columns show the AGV’s first-person RGB observations at the corresponding positions.

Table 4: Performance comparison of w/o perturbation and *GlocDiff* under two levels of noise.

Model			w/o perturbation		<i>GlocDiff</i>		
			$\tau_d(m)$		$\tau_d(m)$		
			0.25	0.35	0.25	0.35	
SR(%) \uparrow	$u_1(m)$	τ_c	10	61.00	69.00	73.00	75.00
			30	73.00	75.00	86.00	88.00
			50	80.00	82.00	92.00	93.00
			∞	86.00	90.00	96.00	96.00
	$u_2(m)$	τ_c	10	42.00	45.00	65.00	65.00
			30	52.00	57.00	69.00	72.00
			50	60.00	65.00	77.00	83.00
			∞	77.00	78.00	86.00	87.00
SPL(%) \uparrow	$u_1(m)$	τ_c	10	42.08	46.38	53.95	57.39
			30	57.15	60.80	61.86	65.61
			50	61.79	62.24	64.84	68.79
			∞	63.41	65.82	65.63	69.58
	$u_2(m)$	τ_c	10	29.90	33.38	44.40	44.40
			30	34.41	39.93	52.07	56.77
			50	37.73	40.84	57.23	59.21
			∞	41.61	46.19	61.14	63.75

guidance. Third, when τ_c approaches infinity, the w/o path model surprisingly incurs more collisions than the w/o depth variant, which appears counterintuitive. We hypothesize that the absence of shortest path guidance compels the agent to follow unnecessarily prolonged and circuitous trajectories, thereby increasing the likelihood of collisions.

We select two episodes, each from a different unseen scene, and visualize the results in Fig. 5. When the agent navigates to the same goal, different models generate distinct actions due to their varying capabilities. The w/o depth model encounters collisions with walls and furniture in both cases, indicating the role of local guidance in generating collision-free navigation actions. In *Mobridge*, the w/o path model generates incorrect actions at the intersection due to the lack of guidance from the optimal path.

Ablation Study on GT Perturbation We retrain our model with the GT perturbation trick removed and refer to this revised version as w/o perturbation. We then assess the robustness of *GlocDiff* and w/o perturbation to localization noise across ten unseen environments. Specifically, we introduce two levels of noise, $u_1(m) \sim \mathcal{U}(0.0, 0.5)$ and $u_2(m) \sim \mathcal{U}(1.0, 2.0)$, to the GT localization results and evaluate the performance of *GlocDiff* and w/o perturbation under both conditions. As shown in Tab. 4, *GlocDiff* outperforms w/o perturbation across all conditions, and the performance of w/o perturbation degrades more severely than that of *GlocDiff* as the noise level increases. This highlights that

incorporating noise during training significantly enhances the model’s robustness to localization errors.

Real World Deployment

This section presents the results of deploying the *GlocDiff* on an AGV in a real apartment without any fine-tuning. The AGV is equipped with a mobile base, an RGB camera, and an NVIDIA Jetson AGX Orin for model execution. We scan the apartment using Scaniverse and apply post-processing to generate a floor plan with characteristics consistent with those in the dataset. For reliable localization, we employ the AGV’s single-line LiDAR-based odometry for pose estimation, with the robot’s initial pose pre-calibrated to ensure stable performance. On the Orin device, the model achieves an inference speed of approximately 1.21Hz. The actions generated by *GlocDiff* are converted into linear and angular velocities via a PD controller.

We evaluate the system on 10 episodes, with $\tau_c = 0$ and $\tau_d = 20\text{cm}$. Each pair is tested three times to ensure reliability, resulting in a final success rate of 40%. Fig. 6 showcases three navigation episodes, highlighting the generalization of obstacle avoidance and planning capabilities to unseen real-world environments. Please refer to the attached demo for a more intuitive illustration.

Conclusion

In summary, we propose an efficient and practical visual navigation framework based on floor plans, leveraging local and global condition extraction alongside a diffusion policy. Our method addresses the challenge of efficiently integrating visual information with the floor plan for optimal path planning. Meanwhile, visual odometry ensures stable localization, enhancing real-world applicability. Looking forward, we foresee the integration of multi-modal data, such as language or object information, further improving adaptability and robustness, paving the way for intelligent indoor service robots in complex environments.

Limitations Despite the promising results, our approach has certain limitations. First, we assume a consistent scale between the floor plan and the real-world environment. However, in real scenarios, floor plans may exhibit distortions or scale mismatches, which could undermine navigation accuracy. Second, although our diffusion-based policy improves the agent’s obstacle avoidance ability, it still cannot guarantee fully collision-free behavior. To enable reliable deployment in practical applications, this issue must be further addressed.

References

- Boniardi, F.; Valada, A.; Mohan, R.; Caselitz, T.; and Burgard, W. 2019. Robot Localization in Floor Plans Using a Room Layout Edge Extraction Network. In *International Conference on Intelligent Robots and Systems (IROS)*.
- Chaplot, D. S.; Gandhi, D. P.; Gupta, A.; and Salakhutdinov, R. R. 2020a. Object Goal Navigation using Goal-Oriented Semantic Exploration. In *Advances in Neural Information Processing Systems (NeurIPS)*.
- Chaplot, D. S.; Salakhutdinov, R.; Gupta, A.; and Gupta, S. 2020b. Neural Topological SLAM for Visual Navigation. In *Conference on Computer Vision and Pattern Recognition (CVPR)*.
- Chen, C.; Wang, R.; Vogel, C.; and Pollefeys, M. 2024. F³Loc: Fusion and Filtering for Floorplan Localization. In *Conference on Computer Vision and Pattern Recognition (CVPR)*.
- Chen, J.; Lin, B.; Liu, X.; Ma, L.; Liang, X.; and Wong, K.-Y. K. 2025. Affordances-oriented planning using foundation models for continuous vision-language navigation. In *AAAI Conference on Artificial Intelligence (AAAI)*.
- Chen, S.; Guhur, P.-L.; Tapaswi, M.; Schmid, C.; and Laptev, I. 2022. Think Global, Act Local: Dual-Scale Graph Transformer for Vision-and-Language Navigation. In *Conference on Computer Vision and Pattern Recognition (CVPR)*.
- Chi, C.; Feng, S.; Du, Y.; Xu, Z.; Cousineau, E.; Burchfiel, B.; and Song, S. 2023. Diffusion Policy: Visuomotor Policy Learning via Action Diffusion. In *Robotics: Science and Systems (RSS)*.
- Ericson, L.; and Jensfelt, P. 2024. Beyond the Frontier: Predicting Unseen Walls from Occupancy Grids by Learning from Floor Plans. *IEEE Robotics and Automation Letters (RA-L)*, 9(8): 6832–6839.
- Ewe, Z. L.; Chang, F.-H.; Huang, Y.-S.; and Fu, L.-C. 2024. Spatial Graph-Based Localization and Navigation on Scale-less Floorplan. *IEEE Robotics and Automation Letters (RA-L)*, 9(4): 3932–3939.
- Goswami, R.; Sinha, H.; Amith, P.; Hari, J.; Krishnamurthy, P.; Rizzo, J.; and Khorrani, F. 2024. Floor Plan Based Active Global Localization and Navigation Aid for Persons with Blindness and Low Vision. *IEEE Robotics and Automation Letters (RA-L)*, 9(12): 11058–11065.
- Guo, Y.; Sun, J.; Zhang, R.; Jiang, Z.; Mi, Z.; Yao, C.; Ban, X.; and Obaidat, M. S. 2024. An Object-driven Navigation Strategy based on Active Perception and Semantic Association. *IEEE Robotics and Automation Letters (RA-L)*, 9(8): 7110–7117.
- Ho, J.; Jain, A.; and Abbeel, P. 2020. Denoising Diffusion Probabilistic Models. In *Advances in Neural Information Processing Systems (NeurIPS)*.
- Howard-Jenkins, H.; Ruiz-Sarmiento, J.-R.; and Prisacariu, V. A. 2021. LaLaLoc: Latent Layout Localisation in Dynamic, Unvisited Environments. In *International Conference on Computer Vision (ICCV)*.
- Huang, C.; Mees, O.; Zeng, A.; and Burgard, W. 2023. Visual Language Maps for Robot Navigation. In *International Conference on Robotics and Automation (ICRA)*.
- Huang, X.; Chi, Y.; Wang, R.; Li, Z.; Peng, X. B.; Shao, S.; Nikolic, B.; and Sreenath, K. 2024. DiffuseLoco: Real-Time Legged Locomotion Control with Diffusion from Offline Datasets. *arXiv preprint arXiv:2404.19264*.
- Ke, B.; Obukhov, A.; Huang, S.; Metzger, N.; Daudt, R. C.; and Schindler, K. 2024. Repurposing diffusion-based image generators for monocular depth estimation. In *Conference on Computer Vision and Pattern Recognition (CVPR)*.
- Li, J.; Chan, C. L.; Le Chan, J.; Li, Z.; Wan, K. W.; and Yun Yau, W. 2021. Cognitive Navigation for Indoor Environment Using Floorplan. In *International Conference on Intelligent Robots and Systems (IROS)*.
- Li, J.; Huang, W.; Wang, Z.; Liang, W.; Di, H.; and Liu, F. 2025. FloNa: Floor Plan Guided Embodied Visual Navigation. In *AAAI Conference on Artificial Intelligence (AAAI)*.
- Luigi, F. 2025. pySLAM: An Open-Source, Modular, and Extensible Framework for Visual SLAM.
- Mur-Artal, R.; Montiel, J. M. M.; and Tardós, J. D. 2015. ORB-SLAM: A Versatile and Accurate Monocular SLAM System. *Transactions on Robotics (T-RO)*, 31(5): 1147–1163.
- Mur-Artal, R.; and Tardós, J. D. 2017. ORB-SLAM2: An Open-Source SLAM System for Monocular, Stereo, and RGB-D Cameras. *Transactions on Robotics (T-RO)*, 33(5): 1255–1262.
- Nichol, A. Q.; and Dhariwal, P. 2021. Improved denoising diffusion probabilistic models. In *International Conference on Machine Learning (ICML)*.
- Pan, Y.; Xu, Y.; Liu, Z.; and Wang, H. 2025. Planning from imagination: Episodic simulation and episodic memory for vision-and-language navigation. In *AAAI Conference on Artificial Intelligence (AAAI)*.
- Partsey, R.; Wijmans, E.; Yokoyama, N.; Doboşevych, O.; Batra, D.; and Maksymets, O. 2022. Is Mapping Necessary for Realistic PointGoal Navigation? In *Conference on Computer Vision and Pattern Recognition (CVPR)*.
- Ramakrishnan, S. K.; Chaplot, D. S.; Al-Halah, Z.; Malik, J.; and Grauman, K. 2022. PONI: Potential Functions for ObjectGoal Navigation With Interaction-Free Learning. In *Conference on Computer Vision and Pattern Recognition (CVPR)*.
- Ronneberger, O.; Fischer, P.; and Brox, T. 2015. U-net: Convolutional networks for biomedical image segmentation. In *International Conference on Medical Image Computing and Computer-Assisted Intervention (MICCAI)*.
- Setalaphruk, V.; Ueno, A.; Kume, I.; Kono, Y.; and Kidode, M. 2003. Robot navigation in corridor environments using a sketch floor map. In *International Symposium on Computational Intelligence in Robotics and Automation*.
- Simeonov, A.; Goyal, A.; Manuelli, L.; Yen-Chen, L.; Sarmiento, A.; Rodriguez, A.; Agrawal, P.; and Fox, D. 2023. Shelving, Stacking, Hanging: Relational Pose Diffusion for Multi-modal Rearrangement. In *Conference on Robot Learning (CoRL)*.
- Sridhar, A.; Shah, D.; Glossop, C.; and Levine, S. 2024. NoMaD: Goal Masked Diffusion Policies for Navigation and Exploration. In *International Conference on Robotics and Automation (ICRA)*.

Tan, M.; and Le, Q. 2019. Efficientnet: Rethinking model scaling for convolutional neural networks. In *International Conference on Machine Learning (ICML)*.

Wang, H.; Liang, W.; Van Gool, L.; and Wang, W. 2023. DREAMWALKER: Mental Planning for Continuous Vision-Language Navigation. In *International Conference on Computer Vision (ICCV)*.

Waswani, A.; Shazeer, N.; Parmar, N.; Uszkoreit, J.; Jones, L.; Gomez, A.; Kaiser, L.; and Polosukhin, I. 2017. Attention is all you need. In *Advances in Neural Information Processing Systems (NeurIPS)*.

Wijmans, E.; Kadian, A.; Morcos, A.; Lee, S.; Essa, I.; Parikh, D.; Savva, M.; and Batra, D. 2020. DD-PPO: Learning Near-Perfect PointGoal Navigators from 2.5 Billion Frames. In *International Conference on Learning Representations (ICLR)*.

Xia, F.; Zamir, A. R.; He, Z.; Sax, A.; Malik, J.; and Savarese, S. 2018. Gibson env: Real-world perception for embodied agents. In *Conference on Computer Vision and Pattern Recognition (CVPR)*.

Yokoyama, N.; Ha, S.; Batra, D.; Wang, J.; and Bucher, B. 2024. VLFM: Vision-Language Frontier Maps for Zero-Shot Semantic Navigation. In *International Conference on Robotics and Automation (ICRA)*.

Yu, X.; Zhang, S.; Song, X.; Qin, X.; and Jiang, S. 2024. Trajectory diffusion for objectgoal navigation.

Zhao, X.; Agrawal, H.; Batra, D.; and Schwing, A. G. 2021. The Surprising Effectiveness of Visual Odometry Techniques for Embodied PointGoal Navigation. In *International Conference on Computer Vision (ICCV)*.

Zheng, D.; Huang, S.; Zhao, L.; Zhong, Y.; and Wang, L. 2024. Towards Learning a Generalist Model for Embodied Navigation. In *Conference on Computer Vision and Pattern Recognition (CVPR)*.

Zhou, G.; Hong, Y.; and Wu, Q. 2024. Navgpt: Explicit reasoning in vision-and-language navigation with large language models. In *AAAI Conference on Artificial Intelligence (AAAI)*.

Floor Plan-Guided Visual Navigation Incorporating Depth and Directional Cues (Supplementary Material)

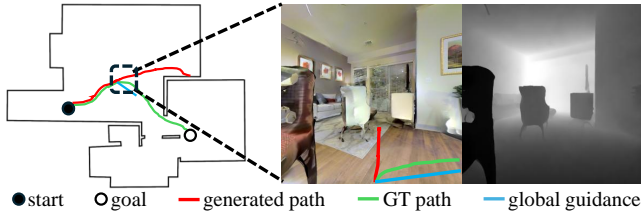


Figure A1: **Failure case.** The left column presents the GT path and the generated path on the floor plan. The right column showcases an RGB observation along with the predicted depth and visualizes the GT path, the generated path, and the shortest path on the observation.

Table A1: Error Comparison of Localization Methods

localization method	Translation (m)			Orientation ($^{\circ}$)		
	mean	median	max	mean	median	max
VO	1.53	1.66	4.28	13.35	18.72	22.51
F ³ Loc	3.44	2.17	9.47	18.14	17.96	30.64

Failure Case

Fig. A1 illustrates a typical failure case where our model generates a path (red line) that deviates from the optimal path (green line), despite the global guidance (blue line) being correct. This occurs because, from current viewpoint, the region suggested by global guidance exhibits low depth. Consequently, *GlocDiff* produces a detour toward a region with higher depth to avoid a perceived collision risk. However, this perceived low depth is merely an illusion caused by the narrow field of view (FOV) and does not reflect that the suggested area is truly impassable. This indicates that a larger FOV could help generate more accurate actions.

Performance of VO and F³Loc

We additionally evaluate the accuracy of two localization modules, *i.e.* VO (Luigi 2025) and F³Loc (Chen et al. 2024). The input images for localization are of size $512 \times 512 \times 3$, with both the vertical and horizontal fields of view set to 90 degrees. We employ the multi-frame inference mode of the pre-trained F³Loc model to estimate camera poses. For VO, we initialize the camera pose of the first frame using the ground truth. Due to the lack of an absolute scale, we manually specify the initial displacement between the first and second frames as 0.04 m, corresponding to the average inter-frame motion observed in our dataset. We randomly sample a total of fifty episodes from ten scenes and compute the mean and median errors between the predicted and ground-truth poses at each time step. As shown in Tab. A1, VO demonstrates a higher average accuracy compared to F³Loc. Moreover, F³Loc exhibits occasional outliers, suggesting that its estimated poses abruptly jump to distant locations within the environment. Such discontinuous pose estimations are intolerable for *GlocDiff*. In contrast, although VO is susceptible to cumulative drift, the noise introduced remains within a range that *GlocDiff* can robustly tolerate, making VO a more suitable choice in practice.

Table A2: Performance Comparison of Different Prediction Horizons on *GlocDiff* (GT).

		Steps			
		16	32	48	
SR(%) \uparrow	τ_c	10	77.40	79.60	79.00
		30	89.80	92.80	91.80
		50	94.00	94.20	94.40
		∞	97.80	97.60	97.40
SPL(%) \uparrow	τ_c	10	62.69	66.60	65.00
		30	67.83	70.38	69.09
		50	68.62	70.98	70.32
		∞	71.89	72.36	72.23

Ablation on Prediction Horizon

We examine how different action prediction horizons affect the performance of *GlocDiff* (GT). Specifically, we evaluate three configurations with prediction lengths of 16, 32, and 48 steps. All models are trained for 20 epochs until convergence. We evaluate all three models using a fixed distance threshold $\tau_d = 0.25$, and vary the intervention count threshold τ_c among 10, 30, 50, ∞ . According to Tab. A2, all three configurations yield comparable performance, with the 32-step model performing slightly better. Thus, we select a prediction horizon of 32 steps for evaluation.